

# Radio, EUV, and X-Ray Observations During a Filament Rise in the 2011 June 7 Solar Flare

MARIAN KARLICKÝ,<sup>1</sup> JANA KAŠPAROVÁ,<sup>1</sup> AND ROBERT SYCH<sup>2</sup>

<sup>1</sup>*Astronomical Institute of the Czech Academy of Sciences, Fričova 298, Ondřejov, 251 65, Czech Republic*

<sup>2</sup>*Institute of Solar-Terrestrial Physics SB RAS, Irkutsk, Russia*

(Received 2019 August 21; Revised 2019 November 12; Accepted 2019 November 13)

## ABSTRACT

The most energetic flares start with a filament rise followed by magnetic reconnection below this filament. The start of the reconnection corresponds to the beginning of the flare impulsive phase. In this paper we study processes before this phase. During the filament rise we recognize an unusual radio continuum with a starting boundary drifting toward lower frequencies. The estimated velocity of the agent generating this continuum boundary is about 400 km s<sup>-1</sup>, similar to that of the rising filament. In association with this filament rise, transient X-ray sources and extreme ultraviolet (EUV) brightenings are found near the filament footpoint and outside the locations where later two parallel flare ribbons appear. Moreover, oscillations with a  $\sim 30$  s period are found simultaneously in radio, EUV, and X-ray observations. Around the end of these oscillations the flare impulsive phase starts as seen in observations of the drifting pulsation structure and X-ray source located at the upper part of the rising filament. We interpret the unusual radio continuum and transient X-ray sources, which are located outside the two parallel flare ribbons, as those generated during an interaction of the rising filament with the above-lying magnetic loops. The EUV brightening at the filament footpoint could be a signature of the magnetic reconnection inside the magnetic rope carrying the filament. Possible scenarios of the  $\sim 30$  s period oscillations in radio, X-ray, and EUV are discussed.

**Keywords:** plasmas – Sun: flares – Sun: radio radiation – Sun: oscillations – Sun: EUV radiation – Sun: X-rays, gamma rays

## 1. INTRODUCTION

As expressed in a three-dimensional model of two-ribbon flares, these flares start with a filament eruption (Aulanier et al. 2012, 2013). While the evolution of such flares during and after their impulsive phase has been studied in many papers (for review see, e.g., Fletcher et al. 2011), the very early phase just after the start of the filament rise and before the impulsive phase is still not well understood. This is due to the fact that this phase is usually relatively short. However, in the 2011 June 7 flare associated with the ejection of an unusually huge filament, this pre-impulsive phase was relatively long, i.e. nearly 10 minutes. This flare had already been studied in several papers. For example, Cheng et al. (2012) studied the formation of extreme

ultraviolet (EUV) wave from the expansion of a coronal mass ejection (CME). They found that, following the solar eruption onset, the CME exhibits a strong lateral expansion and the expansion speed of the CME bubble increases from 100 km s<sup>-1</sup> to 450 km s<sup>-1</sup> in only six minutes. Inglis & Gilbert (2013) studied motions of the X-ray and UV sources at times starting with the flare impulsive phase at 06:25 UT. They described substantial parallel and perpendicular motion of the hard X-ray footpoints. The motion of the footpoints parallel to the flare ribbons is unusual; it reverses direction on at least two occasions. van Driel-Gesztelyi et al. (2014) investigated the coronal magnetic reconnection driven by the CME. They presented observations together with a data-constrained numerical simulation, demonstrating the formation/intensification of current sheets along a hyperbolic flux tube at the interface between the CME and the neighboring active region. Yardley et al. (2016) studied a flux cancellation during the filament eruption. There are also the papers describing filament blobs in

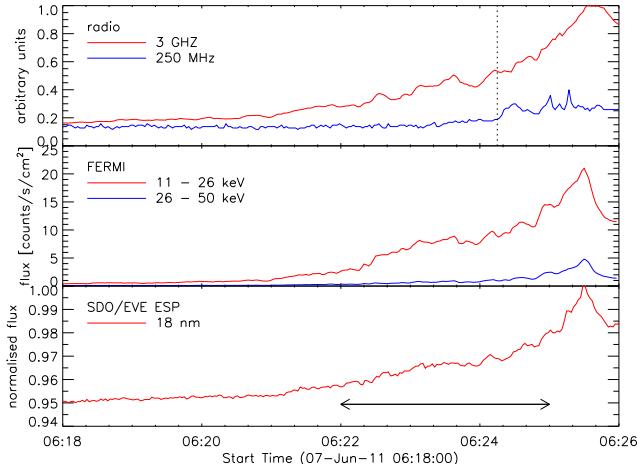


**Figure 1.** Light curves of *Fermi*/GBM detector No. 5, EVE/ESP 18 nm, and radio emission at 3 GHz and 250 MHz. For display purposes, these data were rebinned to a 2s time resolution. The vertical line in radio denotes the start of the drifting pulsation structure (start of the flare impulsive phase). The horizontal line with arrows indicates the interval of the  $\sim 30$  s oscillations, approximately.

this filament eruption, especially those falling back to the Sun (Innes et al. 2012, 2016; Gilbert et al. 2013; Carlyle et al. 2014).

The main purpose of this paper is to investigate in detail the relatively long pre-impulsive phase of the 2011 June 7 flare (SOL2011-06-07T06:16). We present an unusual radio continuum observed at this phase together with transient X-ray sources and the oscillations, recognized simultaneously in hard X-ray, EUV, and radio emissions. For analysis of these oscillations we use not only the well known wavelet power spectra (see, e.g., Ireland et al. 2015; Hayes et al. 2016), but also the wavelet amplitude spectra. While the wavelet power spectrum expresses the square of the absolute value of the wavelet coefficients, the wavelet amplitude spectrum corresponds to the real part of the wavelet coefficients (Astaf’eva 1996; Sych & Yan 2002; Sych & Nakariakov 2008). Although the wavelet amplitude spectra are not frequently used by the solar physics community, we consider them to be very useful because they show not only periods but also phases of the oscillations. We also use these spectra for an analysis of the relationship between different light curves, applying the wavelet coherence and wavelet cross-correlation digital techniques. Microwave observations from Nobeyama radioheliograph and radio polarimeters are also analyzed. Finally, all observations are discussed and a scenario for the pre-impulsive flare phase is suggested.

## 2. OBSERVATIONS AND ANALYSIS

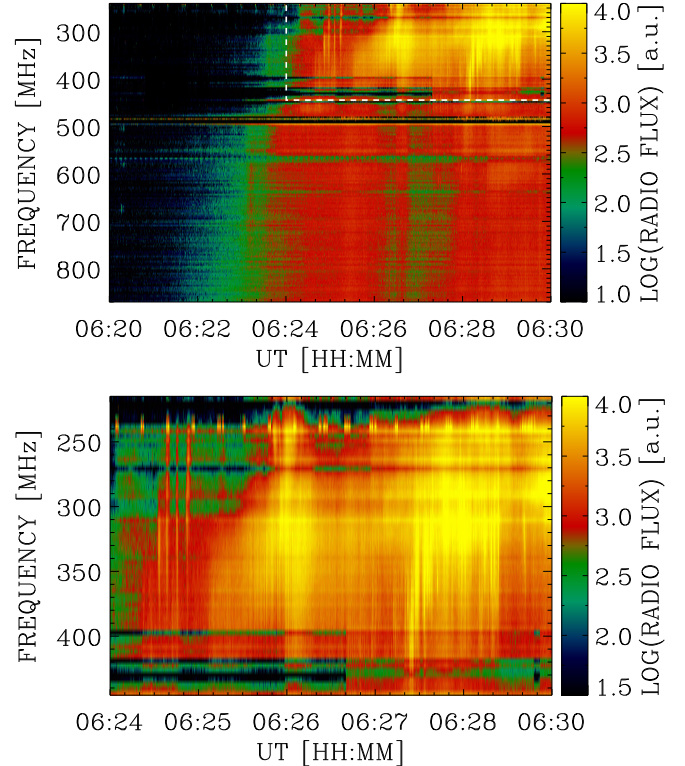


**Figure 2.** Top: BLEN7M-Callisto radio spectrum observed on 2011 June 7, showing an unusual continuum which starts at 870 MHz at about 06:21:40 UT and whose starting boundary drifts from high to low frequencies. This emission is followed by the drifting pulsation structure (DPS) observed in the 220–450 MHz range at about 06:24:15–06:30 UT. Bottom: zoom of the spectrum with DPS, corresponding to the box delineated by the dashed line in the top panel.

In the active region NOAA 11226, on 2011 June 7, an M2.5 class flare was observed at the location of S22°W53°. It started at 06:16 UT with the eruption of a massive filament.

The light curves of the pre-impulsive phase of this flare in X-rays (*Fermi* Gamma-Ray Burst Monitor (*Fermi*/GBM); Meegan et al. 2009), EUV (EUV Experiment (EVE/ESP); Woods et al. 2012) and radio (3 GHz radiotelescope; Jiříčka et al. 1993; BLEN7M-Callisto; Benz et al. 2005 at 250 MHz) are shown in Fig. 1. As can be seen, the emission in all bands increases up to the first peak at 06:25:30 UT and the light curves show quasi-periodic pulsations. The impulsive phase in radio emission started at about 06:24:15 UT as shown by the vertical dashed line.

### 2.1. Radio observations

Figure 2 displays the BLEN7N-Callisto radio spectrum of the beginning of the 2011 June 7 flare (Benz et al. 2005). (We note that a similar spectrum was also

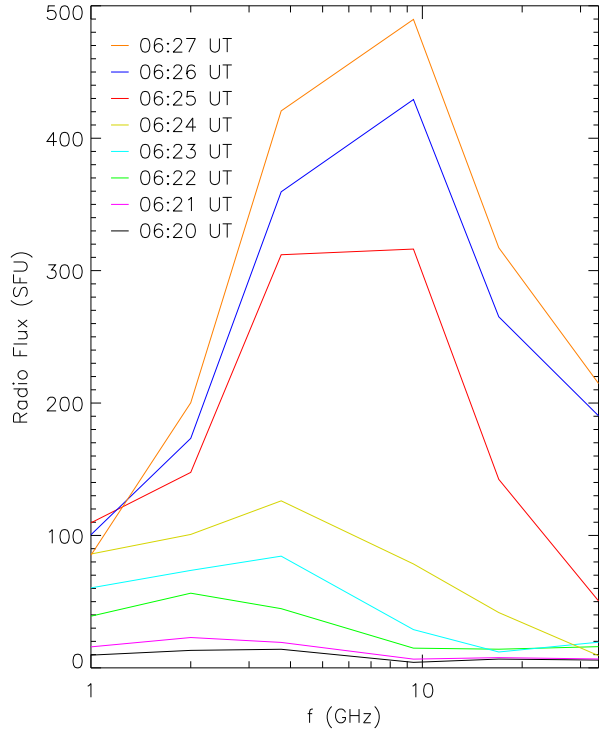


**Figure 3.** Spectra of the flare microwave emission observed by the Nobeyama radio polarimeters from 06:20 UT to 06:27 UT.

observed by OSRA-Callisto at Ondřejov observatory.) As shown, the radio emission starts with the continuum emission whose starting boundary drifts from high to low frequencies. The continuum starts at 870 MHz at about 06:21:40 UT, but at 300 MHz it starts at about 06:24:20 UT. Thus, the mean drift of the starting continuum boundary is about  $-3.6 \text{ MHz s}^{-1}$ . This continuum is unusual. To our knowledge, a similar emission was only observed at the beginning of the 2001 September 24 flare (see Fig. 14 in the paper by Fárnik et al. 2003a), in association with a loop ejection. But the radio emission from that flare was observed at lower frequencies and with a lower frequency drift,  $\sim -0.1 \text{ MHz s}^{-1}$ , than in the present case.

Fig. 2 and its zoom show that this unusual radio continuum is followed by the drifting pulsation structure (DPS), observed in the 220–450 MHz range and at about 06:24:15–06:30 UT. It consists of a series of pulses that as a whole drifts to lower frequencies. DPS is proposed to be a signature of the plasma emission from the plasmoid located in the rising magnetic rope (Kliem et al. 2000; Karlický et al. 2002). Individual pulses in the DPS are generated by superthermal electrons quasi-periodically accelerated in the magnetic reconnection below the ris-

ing filament and trapped in the plasmoid. Because the plasmoid is moving upward in the solar atmosphere, its plasma density decreases and thus the DPS drifts to lower frequencies. We note that this DPS is observed at very low frequencies; usually, they are observed in the GHz frequency range (Nishizuka et al. 2015).

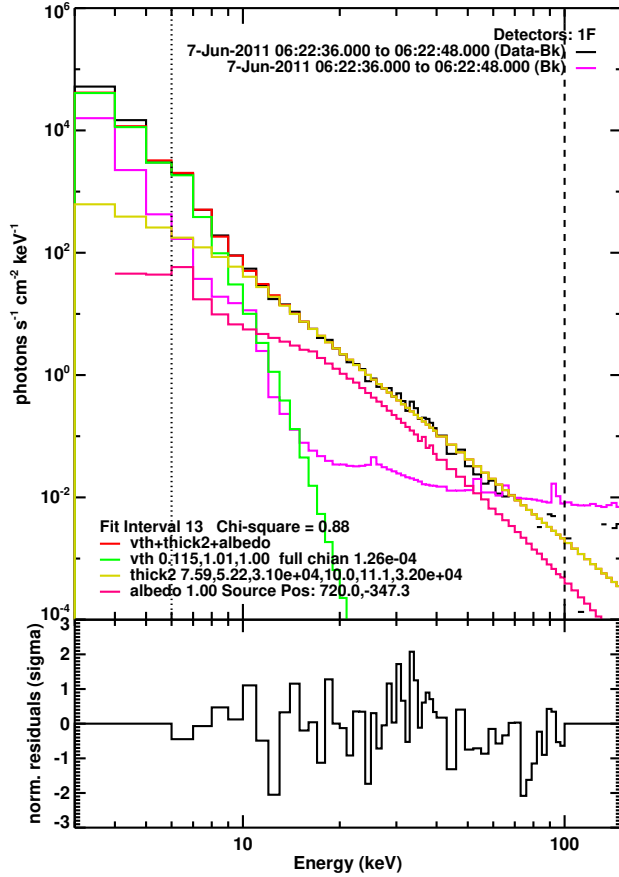
This flare was also observed by the Nobeyama radioheliograph at 17 and 34 GHz (Nakajima et al. 1994) and by the Nobeyama radio polarimeters at six single frequencies: 1, 2, 3.75, 9.4, 17, and 35 GHz (Nakajima et al. 1985). The evolution of the 17 and 34 GHz sources together with the spectral index is shown in a movie available at the Nobeyama radioheliograph page for this event<sup>1</sup>. As can be seen there, the 17 and 34 GHz sources at the position [700, -370] arcsec are extending in time.

Figure 3 shows microwave spectra of this flare obtained from the Nobeyama radio polarimeters data at time 06:20–06:27 UT. At this frequency range the emission is generated by a gyro-synchrotron mechanism. These spectra show a rapid change between 06:24 and 06:25 UT, which corresponds to the start of the flare impulsive phase as indicated also by the start of the DPS.

## 2.2. X-Ray and EUV Observations

We also studied data from *RHESSI* (Lin et al. 2002) and *SDO/AIA* (Lemen et al. 2012). *RHESSI* X-ray sources show complex structure and time evolution on a time scale of several seconds. Therefore, we used *Clean* and *VIS-CS* (Felix et al. 2017) algorithms for X-ray source reconstruction to check hard X-ray (HXR) source positions. The reliability of the image reconstruction was assessed by comparing observed and expected (from the reconstructed image) modulation and visibility profiles, available through the *RHESSI* software. In most cases, both algorithms produced similar results in terms of reconstructed source positions and agreement of the observed and image profiles. However, if the image structure differed significantly between the two algorithms, e.g. if HXR sources were not located within 50% level of the maximum flux, the *Pixon* (Metcalf et al. 1996) algorithm was used as a further check. Other image reconstruction algorithms available in the *RHESSI* software did not produce comparably good agreement of the observed and image profiles. To account for the HXR sources' time evolution, the time interval for the image reconstruction was adjusted so that the total number of counts of the reconstructed image was at least  $10^3$ . HXR images were reconstructed in three energy channels: 6–12, 12–25, and 25–50 keV,

<sup>1</sup> [http://solar.nro.nao.ac.jp/norh/html/event/20110607\\_0627/norh20110607\\_0627.html](http://solar.nro.nao.ac.jp/norh/html/event/20110607_0627/norh20110607_0627.html)



**Figure 4.** *RHESSI* photon spectrum in the 06:22:36–06:22:48 UT time interval fitted with isothermal, albedo, and thick-target components. In the thick-target component the break energy and power-law index above it were fixed to use a single power-law function for this component. The bottom plot shows normalized residuals. Vertical lines denote the energy range used in the fitting.

with the time interval ranging from 28 to 12 s using front grids 4–9. HXR sources reconstructed by *Clean* tend to be larger than those obtained by other algorithms; we did not remove the *RHESSI* instrument point spread function and used the *Clean* default version; see also Dennis & Pernak (2009). On the other hand, *VIS-CS* caused fragmentation of the image in few cases or resulted in artificial sources, i.e. strong sources which were not reconstructed by *Clean* or *Pixon*; see e.g. Figure 6. Generally, *Clean* image modulation profiles showed better agreement with the observed ones for the coarsest (8 and 9) *RHESSI* grids, whereas *VIS-CS* resulted in better agreement for 4–6 grids both in modulation and visibility profiles.

Spatially integrated spectra were analyzed using front detectors 1, 3, 4, 5, 6, 8, and 9 in the 12s time intervals from 06:20:00 UT. Background subtracted spectra were

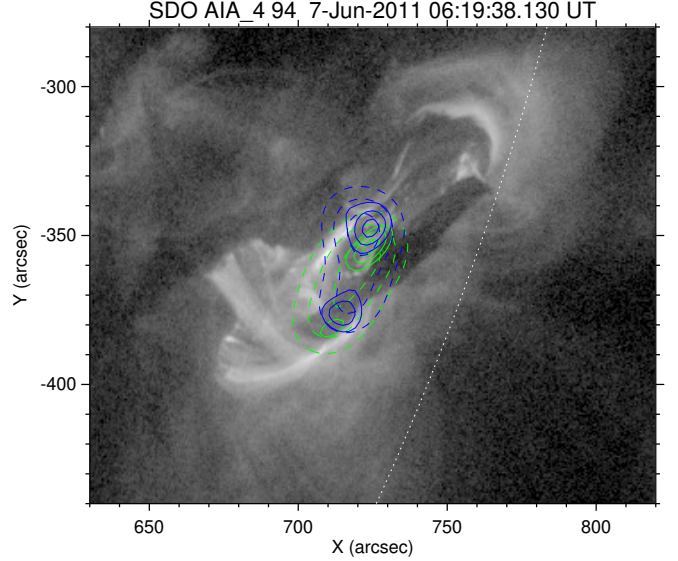


**Figure 5.** *RHESSI* X-ray sources in the 6–12 keV (green) and 12–25 keV (blue) energy ranges in the 06:19:36–06:19:48 UT time interval superposed on the *SDO/AIA* 94 Å image at 06:19:38 UT. Contours correspond to 50, 70, and 90% levels of the maximum in the images. Full lines denote the result obtained by the *VIS-CS* algorithm and dashed lines by *Clean*.

fitted with isothermal, albedo, and thick-target components. The non-thermal component dominated X-ray spectrum above  $\sim 10$  keV, the low-energy cutoff gradually increased from  $\sim 10$  keV at 06:20 UT to  $\sim 15$  keV at 06:26 UT. An example of the fitted *RHESSI* spectrum from detector 1 corresponding to the time interval of the *RHESSI* image in Figure 6 is shown in Figure 4. Therefore, we consider all HXR sources above  $\sim 12$  keV as non-thermal ones produced by accelerated particles.

*SDO/AIA* images were obtained from two sources. First, *SDO/AIA* cutouts were available via `show.synop.pro` interface in SolarSoftWare. These data were not modified. Second, to achieve a higher time resolution in some AIA filters, level 1 data from the JSOC<sup>2</sup> interface were used as well. These were corrected for stray light using the method of Poduval et al. (2013).

Figure 5 shows the X-ray sources (6–12 and 12–25 keV) superposed over the *SDO/AIA* 94 Å image in the very early phase of the filament rise at 06:19:38 UT. At this phase the sources were located along and at the position where at later the two parallel flare ribbons appear. A few minutes later, the distribution of the X-ray sources changed as shown in Figure 6 for 06:22:38 UT,

<sup>2</sup> <http://jsoc.stanford.edu/>



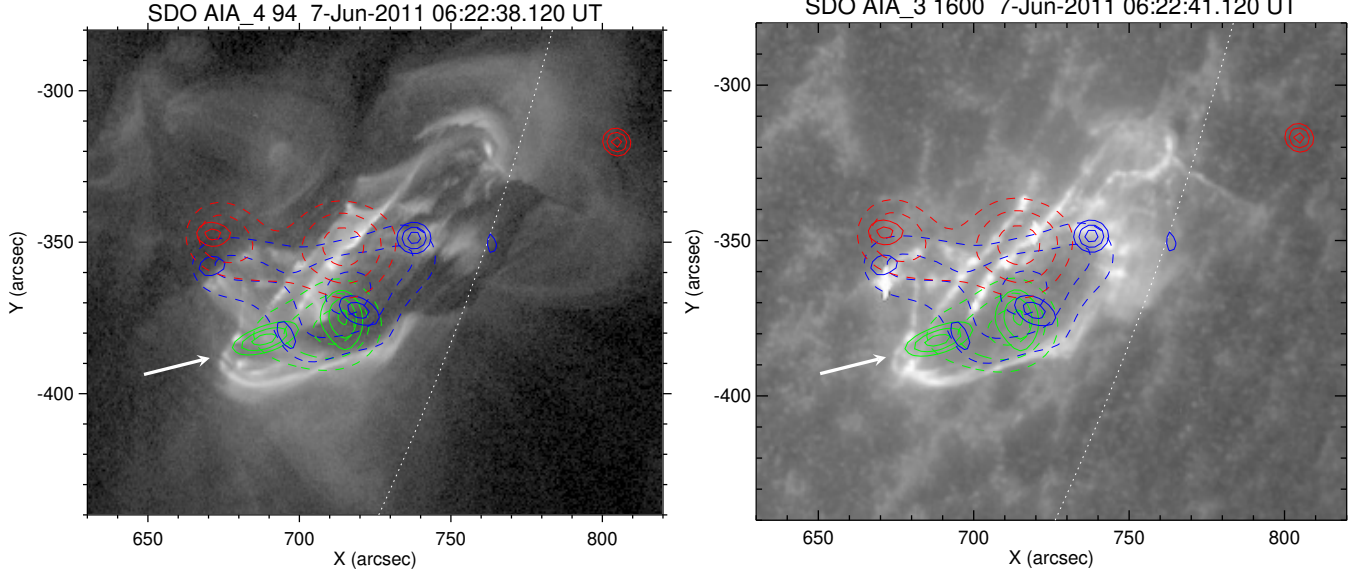


**Figure 6.** *RHESSI* X-ray sources in the 6–12 keV (green), 12–25 keV (blue), and 25–50 keV (red) energy ranges in the 06:22:36–06:22:48 UT time interval superposed on the *SDO/AIA* 94 Å (left) and 1600 Å (right) images at 06:22:38 UT and 06:22:41 UT, respectively. Contours and lines styles are the same as in Fig. 5. The white arrow points to the X-ray source and EUV brightenings at the southern footpoint of the rising filament. The 25–50 keV source on the right edge of the image is probably an artifact.

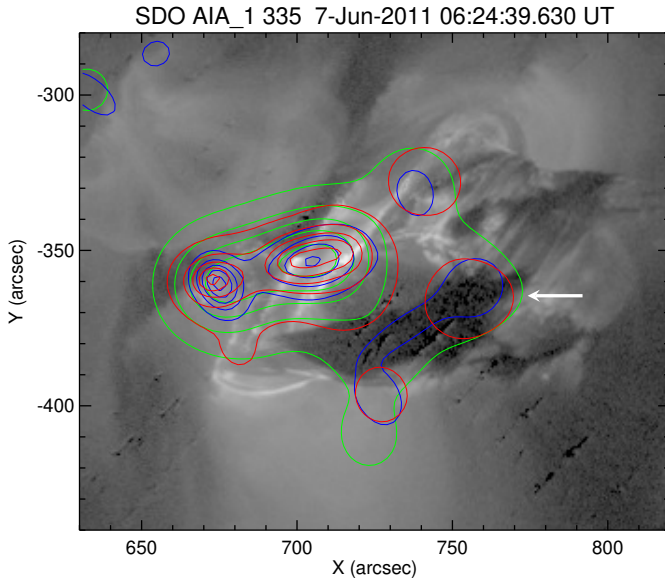


**Figure 7.** *RHESSI* X-ray sources in the 25–50 keV range and in the 06:24:34–06:24:54 UT time interval superposed on the *SDO/AIA* 335 Å image at 06:24:39 UT. Colours denote the results obtained by three algorithms: *Clean* (green), *VIS-CS* (blue), and *Pixon* (red). Contours correspond to 10, 30, 50, 70, and 90% levels of the maximum in the images. The white arrow points to a weak source at the upper part of the filament.

chosen as a representative example. At this phase the X-ray sources are transient in space and time and appear

outside the two ribbons seen in EUV emission, mainly around the southern part of the rising filament. The arrow in this figure points to the X-ray source and EUV brightenings at the footpoint of the rising filament (part of the rising magnetic rope). The phase ends at the beginning of the flare impulsive phase at 06:24:15 UT as shown by the start of the DPS (Figure 2) and by a rapid increase of the microwave spectrum between 06:24 and 06:25 UT (Figure 3). Because the DPS is expected to be the radio emission from the plasmoid in the magnetic rope (Kliem et al. 2000), we searched for an X-ray source at the upper part of the rising filament. We found such a source at energies above 12 keV and at a position of about [750, -370] arcsec; see the arrow in Figure 7. This X-ray source is rather weak, i.e. apparent only at the 10% level of the maximum flux in the image, yet was reconstructed by all three algorithms used. It occurs at ~06:24:34–06:24:54 UT, and after around ~10 s, disappears. There are two other sources apparent at the 10% level, in the northward [720, -400] and southward [740, -330] directions, but they could be associated respectively with an AIA 1600 Å brightening below the filament leg and an AIA brightening that increases in intensity from 06:24:43 UT e.g. in the 171, 193, and 211 Å AIA filters. Because total image counts in the *RHESSI* images in Figure 7 exceed  $10^4$ , we considered all sources above 10% and appearing in all three algorithms used as real.

Spatially integrated X-ray spectra and their fitted parameters do not show any significant temporal change

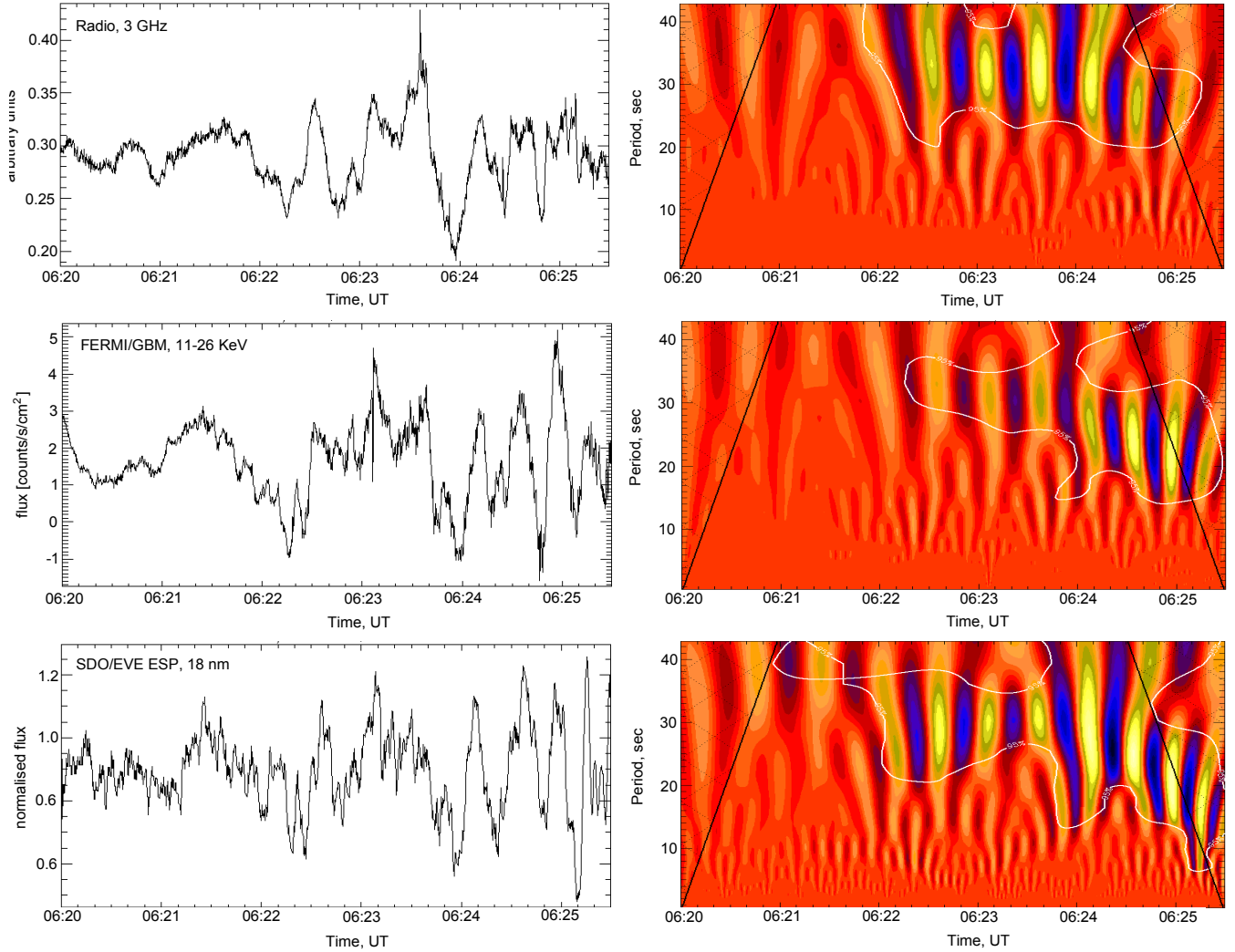


**Figure 8.** Left: detrended light curves of the radio emission (3 GHz), X-ray (*Fermi*/GBM, detector No. 5, 11-26 keV), and EUV (EVE/ESP, 18 nm) for the pre-impulsive phase of the flare, i.e., 06:20:00–06:25:30 UT. Right: wavelet amplitude spectra corresponding to the time profiles on the left. The color background presents the signal variations in time and period. The contour lines indicate the 95% significance level.

while the structures of X-ray sources and radio emission do. The spectra gradually become more intense and extend to higher energies.

### 2.3. Spectral Processing of the Light Curves

As already mentioned, the light curves in X-ray, EUV, and 3 GHz radio emissions indicate quasi-periodic oscillations at the growth phase of the flare. For spectral analysis of the observed periodicity, we used the wavelet transform (Torrence & Compo 1998). Using this technique, we analyzed not only the light curves presented in Figure 1, but also the following data: light curves observed by the two most Sun-directed *Fermi*/GBM detectors, 4 and 5, at energies above 11 keV; *RHESSI* light curves in the 12–25 keV, 25–50 keV, and 50–100 keV en-

ergy ranges; curves obtained by the EVE/ESP experiment in both the 18 nm and 26 nm bands; radio flux profiles at all frequencies (1–35 GHz) of the Nobeyama radio polarimeters; and the correlation curve of the Nobeyama radioheliograph. The time resolution of the 3 GHz radio data was 0.01 s, that of the EUV EVE/ESP data was 0.25 s, and that of the X-ray *Fermi* data was 0.256 s. To compare the curves obtained with different time resolution, we reduced them to the same resolution of 0.25 s using linear interpolation.

In the following we present the results for light curves at radio (3 GHz), X-ray (*Fermi*/GBM, detector No. 5, 11-26 keV), and EUV (EVE/ESP, 18 nm). In the first stage of data preparation we applied the trend removal from the light curves using a six-degree poly-

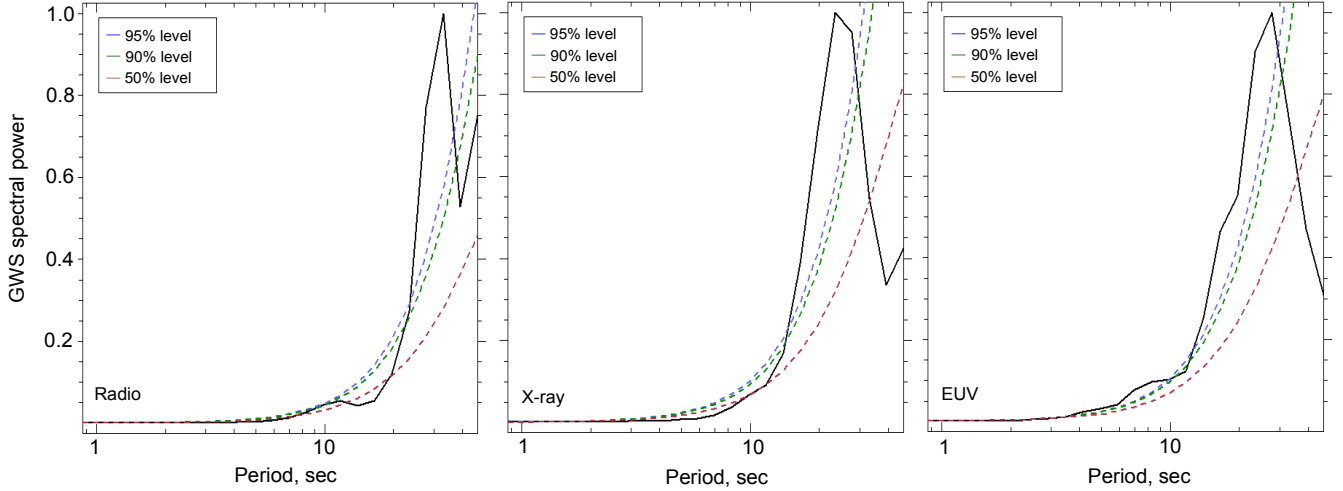


**Figure 9.** Global wavelet spectra for radio, X-ray, and EUV light curves. The broken lines show the 50% (brown), 90% (green), and 95% (blue) significance levels. The spectral power is normalized to the peak level of each spectrum.

nomial approximation. We performed a least-squares polynomial fit of the curves with matrix inversion and optional weighting to determine the fitting coefficients. This allowed us to obtain the detrended curves in the 06:20:00–06:25:30 UT time interval (Fig. 8, left panels). We can see that the signal variance and the corresponding signal-to-noise ratio increase and reach a maximum before the flux peak around 06:25:30 UT. The noise level is insignificant compared to the oscillations, and we can ignore its influence on the signal level. When comparing the profiles, it can be seen that their extremes are almost in phase.

To study the spectral structure of the observed oscillations, we constructed the amplitude wavelet spectra (Fig. 8, right panels) and superimposed the contour with the 95% significance level. To determine the reliability of the found periodicity, we compared them with the background spectra adopting a power-law noise assumption. Then, using a chi-squared distribution we found the 95% significance interval. In our work we applied the software previously used for the pixelised wavelet filtering spectral analysis (Sych & Yan 2002; Sych & Nakariakov 2008; Karlický et al. 2010).

We can see that for the 95% significance level there is a periodicity with an average value near 30 s. There is a drift toward shorter periods with increasing oscillation power. The half-periods of the oscillations, displayed as bright and dark patches, almost coincide in time for the different energy ranges (radio, X-ray, EUV). To obtain a more accurate value of the oscillation periods, we calculated the global wavelet spectra and estimated the 50%, 90%, and 95% significance levels (Fig. 9). The obtained peaks are above the 95% significance level and

correspond to periods of  $\sim 33$  s (radio),  $\sim 25$  s (X-ray), and  $\sim 28$  s (EUV).

To understand how the flare light curves are interconnected at different emissions, we used cross-wavelet analysis and wavelet coherence (Torrence & Compo 1998; Torrence and Webster 1999). These spectral techniques are used to analyze the coherence, cross-correlation, and phase between signals as functions of time and frequency, obtained from the wavelet spectra of two signals. The cross-spectrum is determined by multiplying the wavelet power spectrum of the one signal with the complex conjugate wavelet spectrum of the other. The maximum values of cross-correlation are represented in period-time coordinates and depend on the correlation of oscillation power at certain frequencies. Another method of spectral analysis of two profiles is to construct a wavelet coherence spectrum. This spectrum represents localized amplitudes and phases of correlation wavelet coefficients in the time–frequency domain. The value of the spectra averaged over all times gives us the global coherence and global phase depending on the period. Coherence ranges from 0 to 1, where 0 is the absence of coherence, and 1 is excellent coherence. The global phase range varies from  $180^\circ$  to  $-180^\circ$ .

We prepared the wavelet cross spectra for each pair of the signals (radio–X-ray, radio–EUV, EUV–X-ray) and calculated their global coherences and global phases. It can be seen that (Fig. 10, left panels), for all pairs, the power of cross-oscillations is maximal (cross-correlated) near the  $\sim 30$  s period. Also, simultaneous period drifts toward shorter periods can be seen. This pattern we noted earlier in the analysis of the individual light curves (Fig. 8). Global coherence profiles show a significant

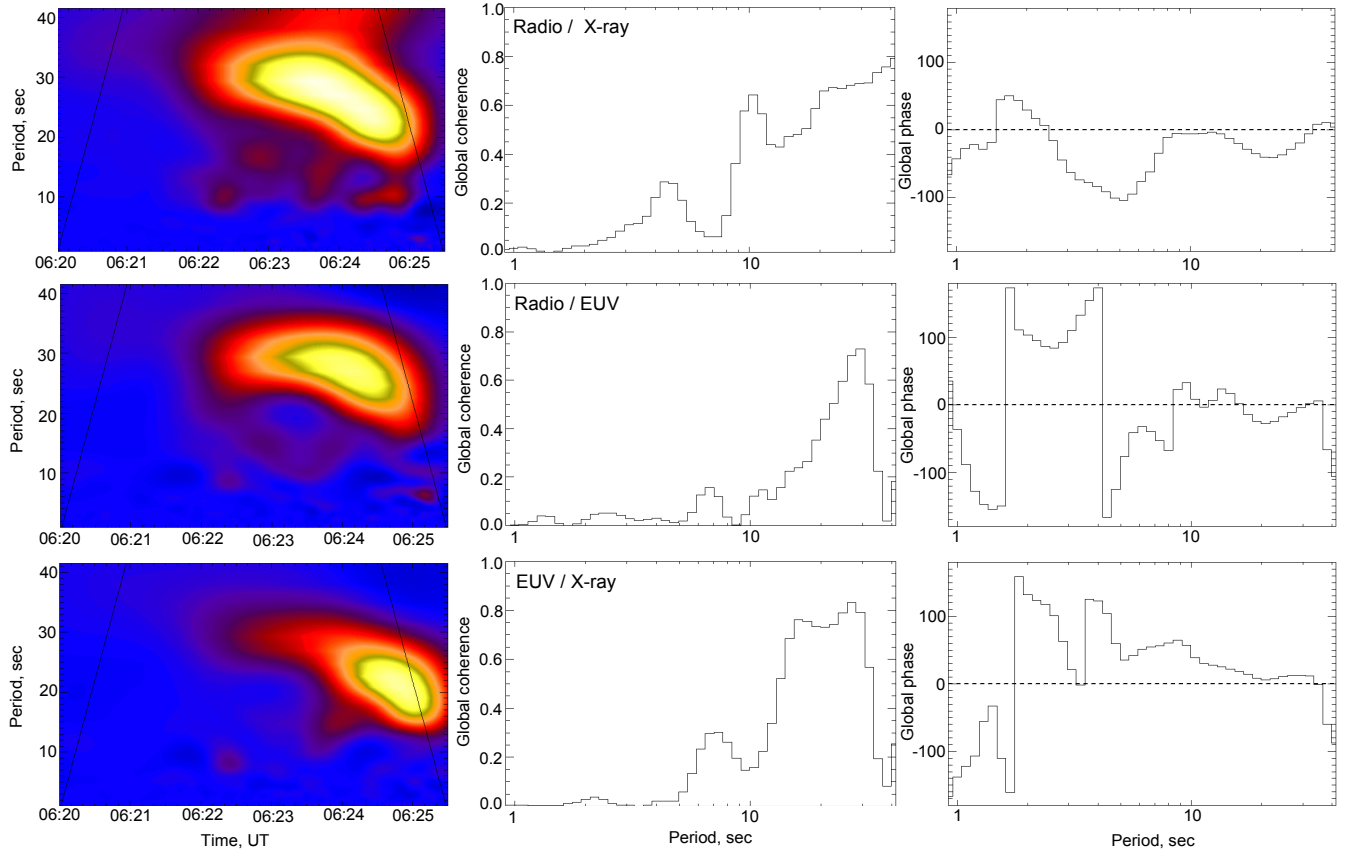


**Figure 10.** Wavelet cross-correlation spectra (left), global coherence profiles (center), and global phase profiles (right) for each pair of the light curves: radio–X-ray, radio–EUV, and EUV–X-ray. The horizontal broken lines show the zero level of the global phase. The coherence is from 0 to 1 and phase from  $-180^\circ$  to  $180^\circ$ .

level of  $\sim 0.7 - 0.8$  for the 30 s periodicity (Fig. 10, central panels). The averaged phase over time of these oscillations is near zero, shown by the broken line, indicating that the signals are in phase (Fig. 10, right panels).

The  $\sim 30$  s period was also recognized in the *RHESSI* channels in the 12–25 and 25–50 keV, *Fermi*/GBM 26–50 keV channels from detectors 4 and 5, in the 26 nm EVE/ESP channel, and in the radio frequencies 2 and 3.75 GHz of the Nobeyama radio polarimeters. Some indication of this period was also found in the correlation curve of the Nobeyama radioheliograph. The found  $\sim 30$  s periodicity with probability 95% for independent instruments indicates the reality of these oscillations. We also searched for the  $\sim 30$  s period at lower radio frequencies, i. e. below 2 GHz, but without result.

In the wavelet amplitude spectra in Figures 8 (right) some vertically long and short striations appear. While the vertically long striations correspond to a very broad interval of periods (therefore no oscillation), the vertically short striations could indicate some further oscillations. But because these further possible oscillations

were recognized only on a few wavelet amplitude spectra, we did not study them in detail. Only the  $\sim 30$  s period was found in nearly all analyzed wavelet amplitude spectra.

In Figure 2 we show also the DPS. Although this DPS could be analyzed as that in Karlický et al. (2018), due to the relatively low temporal resolution (0.25 s) we did not analyze periods in the DPS in detail. As shown in Karlický et al. (2018), the typical periods in DPSs are about 1 s or even fractions of a second. Nevertheless, in the present DPS, the periods in the 4–8 s range were found.

### 3. DISCUSSION AND CONCLUSIONS

We present an unusual radio continuum drifting from higher to lower frequencies, observed during a filament rise. As we already mentioned, to our knowledge only one similar emission has been observed previously, i.e. at the beginning of the 2001 September 24 flare. We call this continuum the rope-rising continuum. Assuming that this continuum is generated by a plasma emission mechanism on the fundamental frequency, and using the



Aschwanden’s model of the solar atmosphere (Aschwanden 2002), the velocity of the agent generating the starting boundary of this continuum is about  $400 \text{ km s}^{-1}$ . This velocity is comparable to that of the rising filament ( $200 - 400 \text{ km s}^{-1}$  (Cheng et al. 2012)). Therefore, we propose that this continuum is generated by the rising magnetic rope in which the filament is embedded. The magnetic rope interacts with the magnetic field above it, and during this interaction (localized reconnections), electrons are accelerated and produce this unusual continuum; see the scenario of flare processes in the pre-impulsive phase in Figure 11. We also note that the upper boundary of the magnetic rope, where the interaction with the above-lying loops takes place, can move upward faster than the filament, owing to the magnetic rope expansion.

We also present a DPS observed on unusually low frequencies (220–450 MHz). Usually they are observed on much higher frequencies in the GHz frequency range (Nishizuka et al. 2015). It seems that this is connected with the eruption of an unusually huge filament. In this case the magnetic reconnection generating the plasmoid and DPS started when the upper part of the magnetic rope, carrying the filament, reached a very high coronal altitude. Because the plasmoid density depends on that of the surrounding plasma, it was lower than usual and thus the plasma emission frequency from the plasmoid (DPS frequency) was unusually low.

As concerns the X-ray sources, we found that at the very beginning of the filament rise the X-ray sources were at a position where later two parallel ribbons appeared in the EUV emission. Then the X-ray sources were transient in space and time and also extended out of the position of these parallel ribbons. We think that the appearance of transient X-ray source located out of the parallel ribbons is also connected with the interaction of the rising magnetic rope and the above-lying magnetic field. The accelerated electrons propagate from the region of interaction along different magnetic field lines downward to different locations, where they heat the plasma (emitting in UV and EUV) and produce transient X-ray emission by thermal and non-thermal bremsstrahlung. Signatures of the complex structure of the above-lying magnetic field can be seen, e.g., in Figure 5 as EUV emission loops perpendicular to the filament with their footpoints at  $\sim [680, -360]$  arcsec.

The phase related to these transient X-ray sources ended during the flare impulsive phase shown by the DPS starting at 06:24:15 UT. The DPS was associated with a sudden increase in the microwave emission and observation of the 25–50 keV X-ray source in the upper part of the rising filament (see the arrow in Fig-

ure 7). We interpret this X-ray source as emission from the plasmoid (Figure 11), which appears as a result of the magnetic reconnection located below the rising filament. But this X-ray source disappeared after a few seconds. We think that this disappearance is by the intensity decrease of this source due to the plasma density decrease in an expanding filament and/or by the intensity increase of other X-ray sources and the relatively low dynamic range of *RHESSI*. After the beginning of the flare impulsive phase, i.e. after 06:26 UT, the X-ray sources appeared at the parallel flare ribbons (Inglis & Gilbert 2013), as usually observed.

In this pre-impulsive flare phase we also found EUV brightenings and the X-ray 6–12 keV source close to the filament footpoint. This agrees with the observation of the hot magnetic rope during the pre-impulsive stage of an eruptive 2012 July 19 flare (Wu et al. 2016). These observations indicate that the plasma is heated and probably also superthermal particles are accelerated in the magnetic rope where the filament is embedded. Such heating and acceleration can be due to the magnetic reconnection inside the magnetic rope where the helical magnetic field is expected. During the rising of this magnetic rope, owing to its kinking, internal reconnection can be triggered. This type of the reconnection can be added to the list of possible types of magnetic reconnection in eruptive flares presented by Aulanier & Dudík (2019) as the rr-rr type.

During the filament rise at about 06:22–06:25 UT we detected  $\sim 30$  s quasi-periodic oscillations simultaneously in hard X-ray, EUV, and 2, 3, 3.75 GHz radio emissions. In global wavelet spectra, peaks in periods above the 95% significance level were found at  $\sim 33$  s (radio),  $\sim 25$  s (X-ray), and  $\sim 28$  s (EUV). There was also a periodicity drift toward shorter periods with increasing oscillation power. The half-periods of oscillations displayed as bright and dark patches almost coincided in time for different energy ranges (radio, X-ray, EUV). Furthermore, the global coherence profiles showed a significant level,  $\sim 0.7$ – $0.8$ , for the  $\sim 30$  s periodicity and the global phase over time of these oscillations was near zero, indicating that the signals with the  $\sim 30$  s period in radio, X-ray, and EUV are in phase.

Oscillations in this flare phase with similar periods are known; see e.g., Fárník et al. (2003b) and Huang et al. (2014). These oscillations can be caused by fast kink mode oscillations as proposed by Huang et al. (2014) or by an oscillatory acceleration/injection process caused by oscillation of the magnetic loop interacting with the rising magnetic rope where the filament is embedded (Nakariakov & Melnikov 2009). Through these interactions (magnetic reconnections) electrons are acceler-

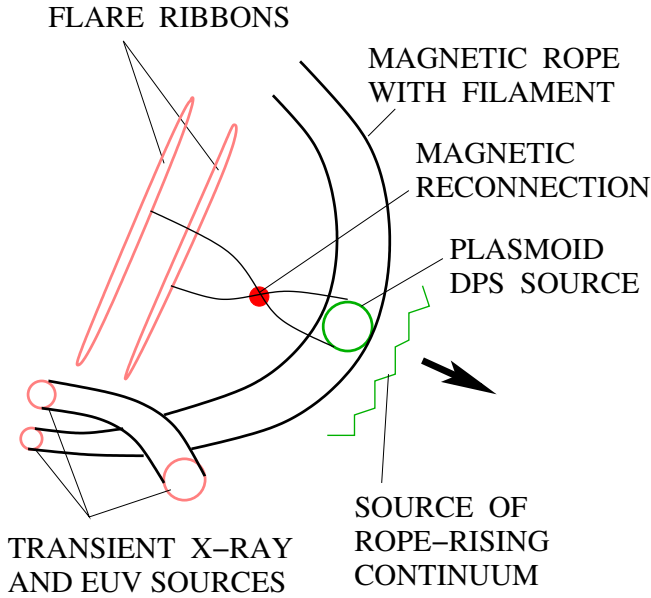


**Figure 11.** Scenario of processes during the filament rise in the 2011 June 7 flare. In the pre-impulsive phase the rope-rising continuum and transient X-ray and EUV sources were generated by the magnetic reconnection between the rising magnetic rope and above-lying magnetic fields as well as by the magnetic reconnection inside the magnetic rope. The impulsive phase started with magnetic reconnection below the rising filament and by the appearance of the DPS and the X-source (plasmoid) at the upper part of the rising filament.

ated and cause the quasi-periodic variations in the observed hard X-ray, EUV, and radio gyro-synchrotron emission. On lower radio frequencies (below 2 GHz), where bursts are preferentially generated by the plasma emission mechanism, no such period was found. It appears that oscillations end due to a much stronger process (magnetic reconnection below the rising filament) in the flare impulsive phase.

Besides the above-mentioned explanations for the oscillation, there is a further possibility: after the interaction of the rising magnetic rope with the above-lying loops, some of the latter are reformed into loops below the rising magnetic rope. During this process a loop starts to oscillate, and moreover, this loop is shrinking. Its period of oscillation can be expressed in the simplest way as

$$P \sim \frac{L}{v}, \quad (1)$$

where  $L$  is the loop length and  $v$  is the characteristic perturbation speed. In our case we assume that  $v = v_A$ , where  $v_A = B/\sqrt{4\pi\rho}$  is the Alfvén velocity,  $B$  is the magnetic field, and  $\rho$  is the plasma density. The plasma density and magnetic field change during the

loop shrinking; therefore, for the oscillation period we can write

$$P \sim \frac{\sqrt{4\pi MV}}{F}, \quad (2)$$

where  $M = \rho V$  is the total plasma mass in the shrinking loop,  $V = LS$  is the loop volume,  $S$  is the loop cross-section area, and  $F = BS$  is the magnetic flux. When we neglect the plasma evaporation in this loop, then  $M$  and  $F$  are conserved during the loop shrinking. Thus, the period of oscillation decreases with the loop volume as  $P \sim \sqrt{V}$ . This interpretation of the observed oscillation is supported by the detected shortening of the oscillation period from about 30 s to 20 s; see Figure 8. In this interpretation it means that the starting loop volume  $V_{\text{start}}$  shrinks to the  $0.44 \times V_{\text{start}}$  at the end of the oscillation. Furthermore, during the loop shrinking the plasma density and magnetic field increase, and so the radio gyro-synchrotron, X-ray, and EUV emissions also increase, as observed. However, verification of this explanation needs further observations and analysis.

Figure 11 summarizes our interpretation of observations of the 2011 June 7 flare. In the pre-impulsive flare phase the rope-rising radio continuum and transient X-ray and EUV sources were generated by magnetic reconnection between the rising magnetic rope and above-lying magnetic fields as well as by magnetic reconnection inside the magnetic rope. The impulsive phase started with magnetic reconnection below the rising filament and by the appearance of a DPS and the X-source (plasmoid) at the upper part of the rising filament.

## ACKNOWLEDGMENTS

The authors thank the referee for comments that improved the paper. M.K. and J.K. acknowledge support from the project RVO:67985815 and GA ČR grants 17-16447S, 18-09072S, and 19-09489S. The study was performed within the basic funding from FR program II.16, RAS program KP19-270, and partially supported by the Russian Foundation for Basic Research (RFBR) under Grant 17-52-80064 BRICS-a. We thank Dr. C. Monstein for the Callisto spectrum, J. Dudík for his help and advice with AIA data, J. Rybák for the help with the radio spectrum, *RHESSI* software and Nobeyama teams. We also acknowledge the use of the *Fermi* Solar Flare Observations facility funded by the *Fermi* GI program (<http://hesperia.gsfc.nasa.gov/fermi.solar/>). AIA data are courtesy of NASA/*SDO* and the AIA science team.

## REFERENCES

- Aschwanden, M. J. 2002, *SSRv*, 101, 1
- Astaf'eva, N. M. 1996, *Physics Uspekhi*, 39, 1085
- Aulanier, G., Démoulin, P., Schrijver, C. J., et al. 2013, *A&A*, 549, A66
- Aulanier, G. & Dudík, J. 2019, *A&A*, 621, A72
- Aulanier, G., Janvier, M., & Schmieder, B. 2012, *A&A*, 543, A110
- Benz, A. O., Monstein, C., & Meyer, H. 2005, *SoPh*, 226, 143
- Carlyle, J., Williams, D. R., van Driel-Gesztelyi, L., et al. 2014, *ApJ*, 782, 87
- Cheng, X., Zhang, J., Olmedo, O., et al. 2012, *ApJL*, 745, L5
- Dennis, B. R., & Pernak, R. L. 2009, *ApJ*, 698, 2131
- Fárník, F., Hudson, H. S., Karlický, M., & Kosugi, T. 2003a, *A&A*, 399, 1159
- Fárník, F., Karlický, M., & Švestka, Z. 2003b, *SoPh*, 218, 183
- Felix, S., Bolzern, R., & Battaglia, M. 2017, *ApJ*, 849, 10
- Fletcher, L., Dennis, B. R., Hudson, H. S., et al. 2011, *SSRv*, 159, 19
- Gilbert, H. R., Inglis, A. R., Mays, M. L., et al. 2013, *ApJL*, 776, L12
- Hayes, L. A., Gallagher, P. T., Dennis, B. R., et al. 2016, *ApJL*, 827, L30
- Huang, J., Tan, B., Zhang, Y., Karlický, M., & Mészáros, H. 2014, *ApJ*, 791, 44
- Inglis, A. R. & Gilbert, H. R. 2013, *ApJ*, 777, 30
- Innes, D. E., Cameron, R. H., Fletcher, L., Inhester, B., & Solanki, S. K. 2012, *A&A*, 540, L10
- Innes, D. E., Heinrich, P., Inhester, B., & Guo, L.-J. 2016, *A&A*, 592, A17
- Ireland, J., McAteer, R. T. J. & Inglis, A. R. 2015, *ApJ*, 798, 1
- Jiříčka, K., Karlický, M., Kepka, O., & Tlamicha, A. 1993, *SoPh*, 147, 203
- Karlický, M., Fárník, F., & Mészáros, H. 2002, *A&A*, 395, 677
- Karlický, M., Zlobec, P. & Mészáros, H. 2010, *SoPh*, 261, 281
- Karlický, M., Rybák, J. & Bárta, M. 2018, *SoPh*, 293, 62
- Kliem, B., Karlický, M., & Benz, A. O. 2000, *A&A*, 360, 715
- Lemen, J. R., Title, A. M., Akin, D. J., et al. 2012, *SoPh*, 275, 17
- Lin, R. P., Dennis, B. R., Hurford, G. J., et al. 2002, *SoPh*, 210, 3
- Meegan, C., Lichti, G., Bhat, P. N., et al. 2009, *ApJ*, 702, 791
- Metcalfe, T. R., Hudson, H. S., Kosugi, T., et al. 1996, *ApJ*, 466, 585
- Nakajima, H., Nishio, M., Enome, S., et al. 1994, *IEEE Proceedings*, 82, 705
- Nakajima, H., Sekiguchi, H., Sawa, M., Kai, K., & Kawashima, S. 1985, *PASJ*, 37, 163
- Nakariakov, V. M. & Melnikov, V. F. 2009, *SSRv*, 149, 119
- Nishizuka, N., Karlický, M., Janvier, M., & Bárta, M. 2015, *ApJ*, 799, 126
- Poduval, B., DeForest, C.E., Schmelz, J.T., & Pathak, S.: 2013, *ApJ*, 765, 144
- Sych, R. A. & Yan, Y. 2002, *ChJA&A*, 2, 183
- Sych, R. A. & Nakariakov, V. M. 2008, *SoPh*, 248, 395
- Torrence, C. & Compo, G. P. 1998, *Bulletin of the American Meteorological Society*, 79, 61
- Torrence, C. & Webster, P. J. 1999, *Journal of Climate*, 12, 2679
- van Driel-Gesztelyi, L., Baker, D., Török, T., et al. 2014, *ApJ*, 788, 85
- Woods, T. N., Eparvier, F. G., Hock, R., et al. 2012, *SoPh*, 275, 115
- Wu, Z., Chen, Y., Huang, G., et al. 2016, *ApJL*, 820, L29
- Yardley, S. L., Green, L. M., Williams, D. R., et al. 2016, *ApJ*, 827, 151